Photoacoustic Raster Scan Imaging Using an Optomechanical Ultrasound Sensor in Silicon Photonics

Cedric Pieters[a,*], Wouter J. Westerveld[a,b], Md. Mahmud-Ul-Hasan[a], Simone Severi[a], Jon Kjellman[a], Roelof Jansen[a], Veronique Rochus[a], and Xavier Rottenberg[a]

[a]Imec, Kapeldreef 75, 3001 Leuven, Belgium
[b]Department of Precision and Microsystems Engineering, Delft University of Technology, 2628 CD Delft, The Netherlands
[*]Corresponding author: cedric.pieters@imec.be

ABSTRACT

To address challenges in ultrasound detection for photoacoustic computed tomography, an optomechanical ultrasound sensor (OMUS) was developed in silicon photonic microchip technology. Such sensors are small (20 µm), sensitive (NEP 1.3 mPa $Hz^{-1/2}$), broadband (measured 3 - 30 MHz), and scalable to a fine-pitch matrix. This optical sensor has extreme sensitivity by combining an acoustic vibrating membrane with an innovative optomechanical waveguide. In this work, we test this sensor for photoacoustic computed tomography (PACT) by measuring and imaging the photoacoustic response of small 10 µm diameter sutures. Sensor signal-to-noise ratio (SNR), image contrast-to-noise ratio (CNR), and image resolution for different sensor geometries are characterized. We conclude that the sensor behaviour is in line with theory and meets the requirements for future applications in photoacoustic tomography.

Keywords: OMUS, photoacoustic imaging, optomechanical sensor, silicon photonics, ultrasound detection, raster scanning tomography, micro ring resonators, optical sensors

1. INTRODUCTION

Photoacoustic imaging is a biomedical imaging modality, where optical absorbers in biological tissue are imaged via pulsed light excitation followed by acoustic detection. It combines the benefits of optic and acoustic imaging modalities by providing rich optical contrast with deeper imaging depths than offered by optical techniques by using ultrasonic focusing.[1–3] Its core strengths and prospects are to provide functional biological information and high spatial/temporal resolution at clinically relevant depths, absent of ionizing radiation.[1] In photoacoustics, biological tissue is illuminated with pulsed laser light, and absorption of light generates broadband acoustic pressure waves via thermoelastic expansion. The pressure waves are detected by acoustic detectors, followed by an image algorithm to image the optical absorbers.[1–3] In current, commercial systems, these acoustic detectors are piezoelectric sensors.[4–6]

Photoacoustic imaging can be further divided into two main imaging modalities: photoacoustic microscopy (PAM) and photoacoustic computed tomography (PACT). PAM provides high resolution images at limited depth. A large focused piezoelectric transducer is used to provide a precise ultrasound detection with a large bandwidth. To image the tissue of interest, the transducer is mechanically raster-scanned over the tissue region of interest, and an ultrasound time-trace is recorded at each position.[4,7] Alternatively, a MEMS scanning mirror can be used for higher scanning speeds.[8] However, mechanical scanning has significant drawbacks: (1) the speed of photoacoustic imaging is often limited by the laser pulse repetition rate, such that the need for a measurement at each scanning position limits imaging speed and (2) the setup is often bulky. In PACT, the ultrasound signals are simultaneously acquired at multiple locations around the tissue of interests and the photoacoustic image is reconstructed by using all these recordings in a computed tomography algorithm.[9] For faithful image reconstruction, obeying Nyquist spatial sampling, these sensors needs to have small pitch, hence a small size of half the acoustical wavelength. However, the noise of piezoelectric sensors scales inversely with their size and this limits their use for high-resolution imaging with small acoustical wavelengths. Consequently, PACT is typically used for imaging with lower resolution than achieved with PAM.[5,10]

To address these limitations, optical ultrasound detectors offer a better sensitivity, detection limit and bandwidth for comparable small footprints.[11] Various optical sensing concepts have been demonstrated with high performance.[11] For instance, optical ultrasound detectors in optical fibers,[12–15] free-space optics,[16] polymer waveguides,[17–19] silicon photonic ring resonators,[20–22] and sub-micrometer sensors at the facet of a photonic chip.[23]

Our recent work has demonstrated a novel, sensitive, small, broadband and scalable optomechanical ultrasound sensor (OMUS). Sensors with a diameter of 20 µm were characterized in the 3-30 MHz frequency range and a detection limit of 1.3 mPa $Hz^{-1/2}$ was found.[24] In this paper, we further study the performance of this OMUS for application in photoacoustic imaging. The signal-to-noise ratio, frequency response and time response of different sized OMUSs are evaluated by measuring photoacoustic signals generated by optically exciting polyamide sutures in water. These sutures are comparable in size to thin vessels found in biological tissue. We then report on photoacoustic computed tomography performed with different sized OMUSs on polyamide sutures in water. From this experiment we evaluate the effect of OMUS size on image contrast and resolution.

2. DEVICE

The OMUS is an optical sensor using light as the information carrier. Laser light is sent through fibers, and coupled to waveguides on a photonic chip where it interacts with incident pressure waves. The pressure waves modulate the transmitted light intensity which are then recorded by a photodetector. In the OMUS, pressure waves deform a membrane. This will modulate the transmitted light intensity of an optical ring resonator. Such a ring resonator consists of a ring-shaped optical waveguide. In the OMUS, an innovative optomechanical waveguide is used that is partly on a fixed substrate and partially on the acoustically vibrating membrane.

A conceptual sketch of the OMUS and cross section of the optomechanical waveguide can be found in figure 1a and 1b, respectively. The optomechanical waveguide consists of a silicon slab and rib part made in silicon photonics. The slab part, shown in pink, is on the suspended membrane and the rib part is placed on the fixed substrate. These parts are separated by a 15 nm gap. Owing to a high electric field intensity inside this gap, a small change in gap height causes a large change in the light's propagation speed, and hence the light's effective wavelength in the waveguide.

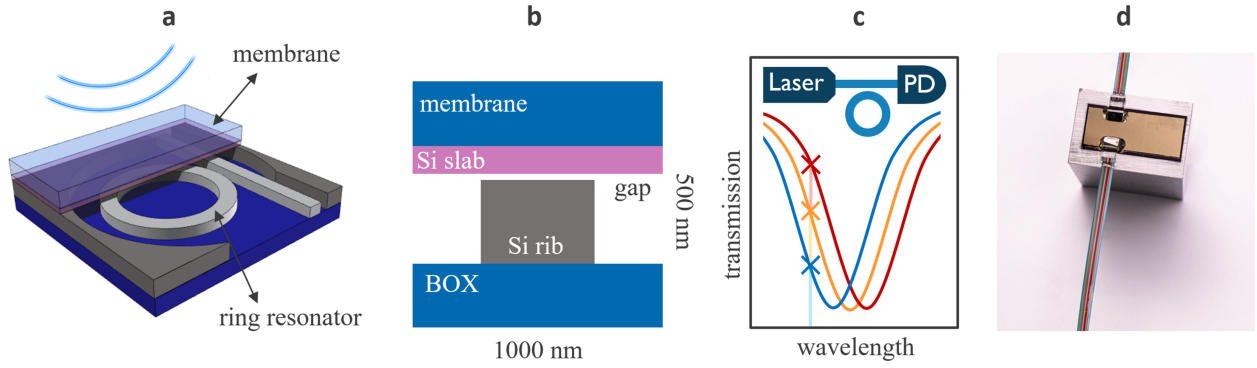

Figure 1. a) Conceptual sketch of OMUS. b) Cross section of the optomechanical waveguide c) Readout principle: a laser is tuned to the resonance flank of the ring resonator. The three optical transmission curves and three crosses correspond to different deflections of the membrane and transmitted light intensity. d) Photograph of the OMUS chip glued on an aluminium block with optical fiber array blocks for optical interrogation of the device.

An optical ring resonator is formed with this optomechanical waveguide. Figure 1c illustrates the ring resonator read-out principle and transmitted light intensity as a function of wavelength. A fixed wavelength continuous wave laser interrogates the ring resonator, and the transmitted light intensity is detected by a photodetector (PD). A ring resonance will occur, when the optical path length is exactly a whole number of wavelengths. As illustrated in 1c, the laser is tuned at the left flank of the ring resonance, at the maximum slope. When the

pressure waves cause the resonance to shift, the light intensity is changed, either to the longer (red) or shorter (blue) wavelengths.

The OMUS modulates light intensity as follows. First, pressure waves impinge on the membrane. Then the membrane vibrates and the gap height changes. This changes the light propagation speed in the waveguide and hence the resonance wavelength of the optical ring resonator. By tuning the laser at the left flank of the ring resonance, the transmitted light intensity changes relative to the acoustic pressure waves. Hence the transmitted laser intensity is a direct measure of the acoustical pressure as a function of time. Figure 1d shows the OMUS chip, which is connected with optical fibers and glued on an aluminium block to reduce acoustic reflection from the backside of the OMUS chip.

3. EXPERIMENTAL SETUP

Figure 2a and 2b illustrate the experimental photoacoustic (PA) setup and a photograph of the setup. A laser generates pulses of green light that illuminates the phantom. For the experiments in this paper, the phantom consists of black polyamide sutures submerged in water. The OMUS, as described in section 2, is positioned above the phantom, mounted to a motorised stage, and interrogated with a tunable continuous wave laser and photodetector. For photoacoustic raster scan imaging, the OMUS was scanned in the x and y directions above the phantom in a 2D planar detection geometry as illustrated in figure 2c. The scanning step size was chosen to be around half the acoustic wavelength of the acoustomechanical resonances of the OMUS to satisfy the spatial Nyquist sampling theorem. Further details on the setup can be found in appendix A.

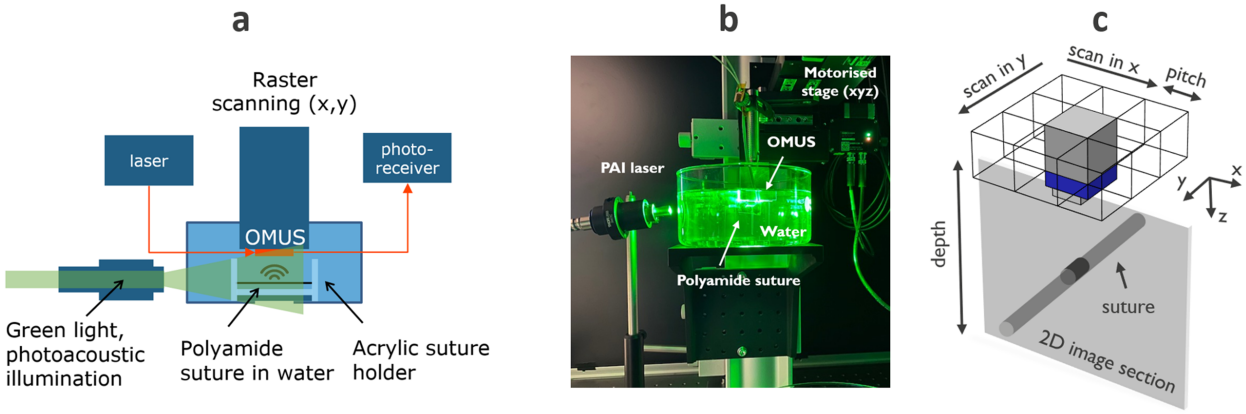

Figure 2. a) Schematic illustration of measurement setup. b) Photo of the photoacoustic setup showing green laser light illuminating the polyamide sutures in water while the OMUS is mounted to a motorised stage. c) Conceptual sketch of the photoacoustic raster scan imaging system. The OMUS records PA signals in a planar detection geometry.

4. SENSOR CHARACTERISATION

To study the difference in sensor response, SNR and resonance frequency between the three different OMUS devices with different membrane sizes, we evaluate the noise amplitude spectral density and the photoacoustic response of a thin vessel-like wire phantom. This phantom was chosen to be a 10 µm polyamide suture submerged in water, sufficiently small in diameter so that it can be regarded as a photoacoustic line source. The three OMUSs of interest have membrane diameters of 25, 21 and 15 µm. The OMUSs were placed at a fixed distance of 2.5 mm above the suture and were measured one at a time. The measured PA signals are shown in figure 3a-c. From these PA signals, the SNR of the sensors was computed as the maximum pressure of the signal divided by the root mean square value of a time trace of the sensor that was recorded without excitation. Only in the measurement of the maximum pressure, the signals were averaged 500 times to get a more precise measurement of the maximum pressure and hence a more precise computation of the SNR. No averaging was applied to the noise. It was found that the SNR is 20.0, 22.7 and 20.0 for the 25, 21 and 15 µm OMUS, respectively. This

indicates that the acquired PA signals by the OMUSs are well above the noise floor. This SNR is sufficient to produce PA images without averaging, as will be shown in section 5.

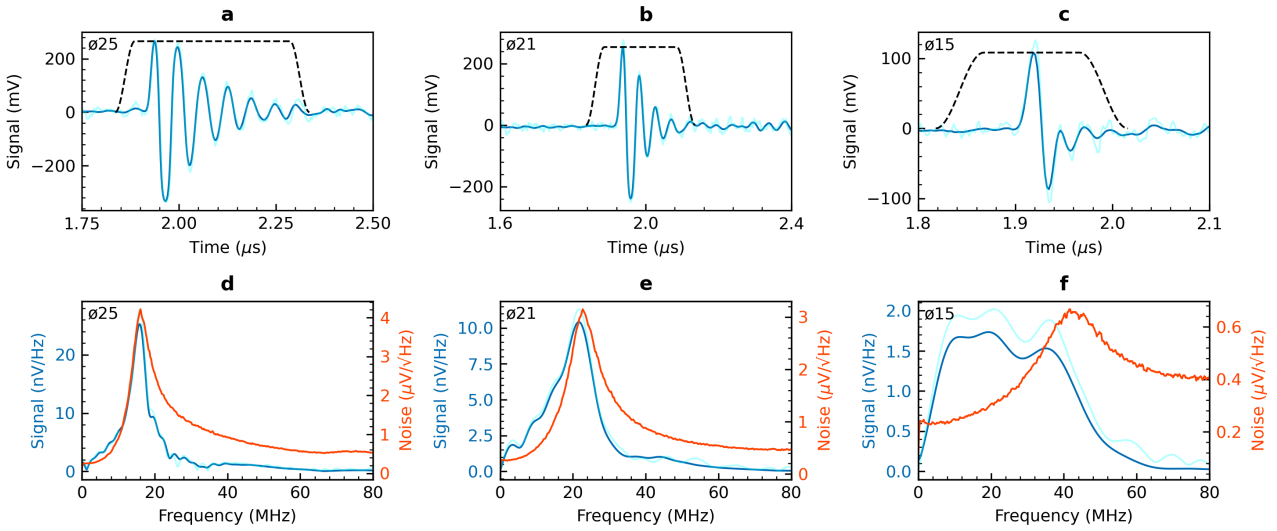

Figure 3. Photoacoustic characterisation of a 10 µm polyamide suture placed at a distance of 2.5 mm below the OMUS. Shown for the three OMUS devices with different membrane diameters. First, second and third column represent the 25, 21 and 15 µm OMUS, respectively (a,b,c) First pulse arrival of the 500 times averaged and unaveraged acquired time traces shown in blue and cyan, respectively. (d,e,f) Signal spectrum in blue and noise amplitude spectral density in orange

The frequency analysis can be found in figure 3d-f and is subdivided into a signal and noise analysis. First, the spectrum of the measured signal was computed, which is affected by the photoacoustic excitation of the suture, propagation of the ultrasound, and receive spectrum of the sensor. The signal spectrum was found by selecting the first pulse arrival with a time-window and then taking a Fourier transform of the signal in this window. Second, to study the OMUS sensor response, the noise amplitude spectral density was measured. This was done by recording time traces absent of pulsed laser excitation, computing the square root of their noise power spectral density.

We used the noise amplitude spectral density to estimate the sensor response. The sources contributing to the noise of the OMUS are electro-optical and acoustomechanical noise. The electro-optical noise is caused by laser noise and PD noise. The acoustomechanical noise stems from membrane vibrations in response to thermal acoustic noise in the water and is much larger than the electro-optical noise.[24] Since the thermal acoustic noise is constant, white noise,[10] the thermal acoustic power in the water is converted to electrical power by the sensor impulse response. Hence, the noise amplitude spectral density, dominated by acoustomechanical noise is a good estimate for the sensor response.

Considering the noise amplitude spectral density as the sensor response estimate, illustrated in orange in figure 3d-f, the acoustic resonance frequencies of the membranes were found to be around 16, 23 and 42 MHz for the 25, 21 and 15 µm OMUS, respectively. The larger membranes have sharp acoustic resonances and are 6.4-3.7 times more sensitive at resonance than the smallest OMUS. We observe, that the bandwidth and acoustic resonance frequencies increase with smaller membrane diameters. Most notable, the fractional bandwidth of the 15 µm OMUS is significantly larger than the larger membranes. These trends are in accordance to acousto-mechanic simulations in COMSOL multiphysics.[24] These results can also be found in table 1.

We observe that the bandwidth of the measured signal spectrum, illustrated in blue in figure 3d-f, is much wider for the smallest, 15 µm OMUS than it is for the larger, 25 and 21 µm OMUSs. We expect that this is caused by the spectrum of the PA signal of the excited suture. Since most energy in the PA signal is located at 40 MHz and frequencies below. Hence, the smallest OMUS, operates below its resonance frequency, where the

sensor response is flatter than around resonance and the larger membranes operate on their acoustic resonance frequencies.

5. PHOTOACOUSTIC IMAGING

5.1 Spatial resolution and contrast-to-noise ratio

To evaluate the difference in spatial resolution and CNR for photoacoustic images measured with the three different OMUSs, photoacoustic imaging is performed on the same 10 µm polyamide suture as in the previous experiment, placed at a depth of 2.5 mm below the OMUS. For this experiment, the OMUSs were raster scanned over an area of $5 \times 5\,\mathrm{mm}^2$, with the suture at the center of the scanning grid. The scanning steps were 37.5, 35 and 18 µm for the 25, 21 and 15 µm OMUS, respectively. These steps were chosen as approximately half the acoustic wavelength of the acoustomechanical resonance frequency of the membranes. At each sensor position, an unaveraged timetrace was recorded, zero-phase filtered in the 3-50 MHz range, and an image was reconstructed using the delay and sum (DAS) algorithm. As a final step, the negative values in DAS were removed and set to zero. To evaluate how well our system can image a thin, small suture in water, a cross section of the 3D resolved suture is taken for the three different OMUSs as illustrated in figure 4a-c. In these images, sharper images are produced by the smaller membranes, but image artifacts are present. These are attributed to the DAS algorithm.

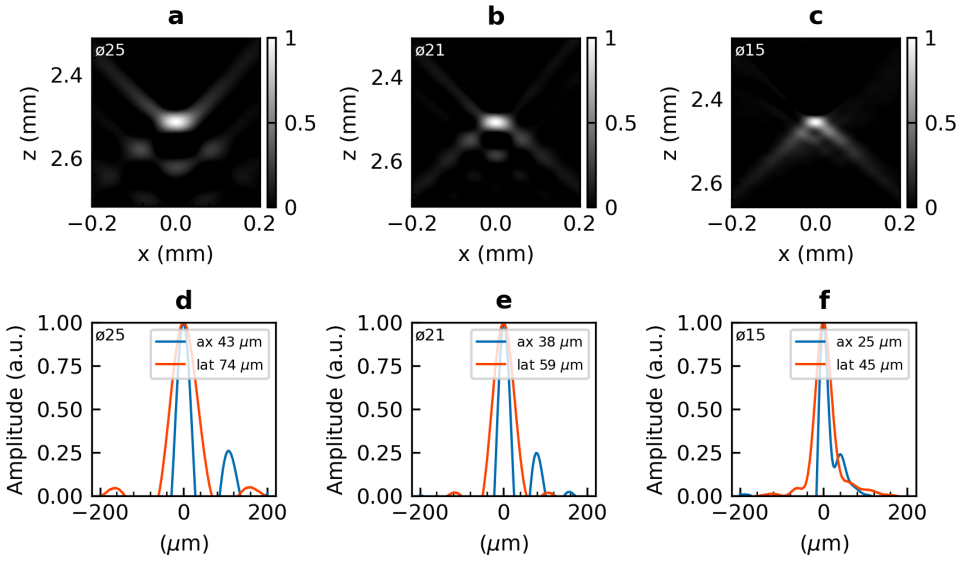

Figure 4. Photoacoustic reconstruction using delay and sum of a 10 µm polyamide suture in water, 2.5 mm below the OMUS. Shown for the three OMUS devices with different membrane diameters. First, second and third column represent the 25, 21 and 15 µm OMUS, respectively (a,b,c) Reconstructed profile of the suture. (d,e,f) Axial and lateral resolution.

To estimate the spatial resolution, the full-width at half-max (fwhm) of the profiles along the z- and x-axis of the suture were taken and illustrated in figure 4d-f. These profiles correspond to the axial and lateral resolution taken from the reconstructed suture images. The CNR was extracted from a 10 µm region of interest (ROI) around the suture. This ROI was compared to an 8 times larger adjacent background region. More details on image algorithm and analysis can be found in B and C, respectively.

A comparison of the three different OMUSs with respect to the membrane diameter, acoustic resonance frequency, bandwidth, spatial resolution and CNR can be found in table 1. First, we consider the resolution of the photoacoustic images. The resolution of the reconstructed suture was 43, 38 and 25 µm in the axial and 74, 59 and 45 µm in the lateral direction for the 25, 21 , and 15 µm OMUS membrane diameter, respectively. The measured spatial resolution is improved with smaller membrane diameters. This trend is expected because the

smaller membranes are more broadband and have higher sensitivity at higher frequencies, such that they can produce images with sharper features. The lateral resolution is affected by the limited detection aperture and DAS algorithm.

Table 1. Comparison table of three different OMUSs using DAS beamforming

OMUS				
Membrane diameter	⌀25	⌀21	⌀15	µm
Center frequency f_0	16	23	42	MHz
-6 dB bandwidth Δf	8.3	12.7	37.5	MHZ
Fractional bandwidth $\Delta f / f_0$	52	55	89	%
Signal SNR	20.0	22.7	20.0	
Measured images				
Axial resolution	43	38	25	µm
Lateral resolution	74	59	45	µm
Image CNR	33.4	50.3	55.1	

We consider the CNR of the images, based on the definition in Appendix C. It can be seen in table 1 that the CNR is higher for the smaller membrane diameters. This is not expected when only considering the sensor detection limit, which is a factor 2 higher for the 15 µm OMUS compared to the 20 µm OMUS.[24] We expect this can be attributed to the following two effects. First, the step size in the raster scanning was chosen smaller for the smaller membrane diameters, hence more recordings are used in the reconstruction of the images with small membrane diameter. Second, there are image artifacts in the image region that is defined as noise region, hence a reduction of these artifacts reduce the noise.

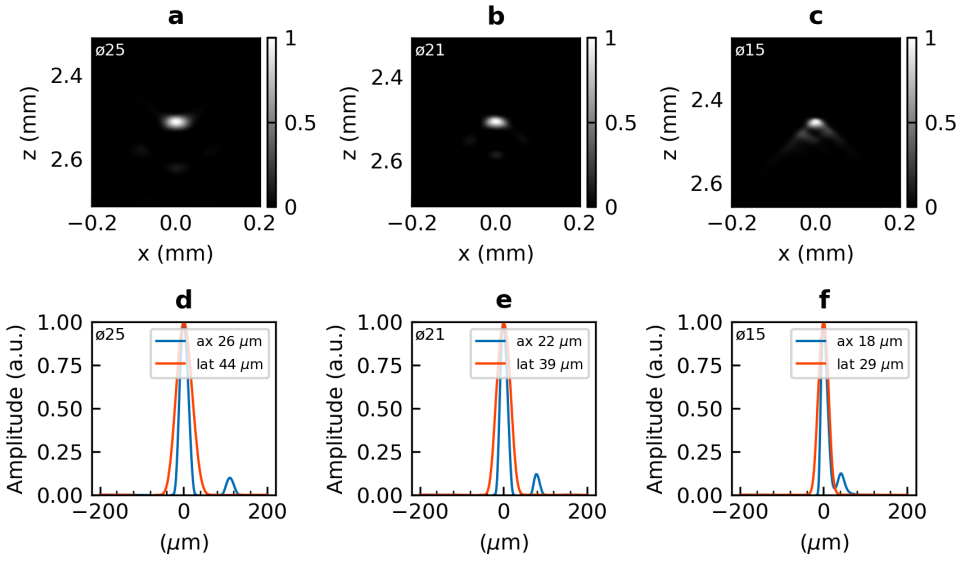

Figure 5. Photoacoustic reconstruction using delay and sum with coherence factor of a 10 µm polyamide suture placed at a distance of 2.5 mm below the OMUS. Shown for the three OMUS devices with different membrane diameters. First, second and third column represent the 25, 21 and 15 µm OMUS, respectively (a,b,c) Reconstructed profile of the suture (d,e,f) Axial and lateral resolution.

To reduce the image artifacts in the images, DAS with coherence factor can be used instead of DAS.[25] This image algorithm multiplies the DAS image with a nonlinear weighting factor to remove the off-axis signal

contribution. In figure 5a-c, this method was applied to reconstruct images with the same experimental data and the corresponding cross-sections along the z- and x- direction are shown in figure 5d-f. It can be seen, that the sidelobes image artifacts are significantly reduced.

5.2 Multi suture phantom in water

To evaluate the photoacoustic performance on a more complex vessel-like phantom, a multi suture phantom was constructed with polyamide sutures of different sizes. Black polyamide sutures were chosen because of its similar acoustic properties to soft tissue. In this experiment, the 21 µm OMUS was raster scanned over an area of $8 \times 8\,\mathrm{mm}^2$ at a step size of 35 µm. The phantom was comprised of three sutures with diameters of 150, 50 and 10 µm held in place by an acrylic suture holder shown in figure 6a. To reduce image artifacts, the DAS with coherence factor algorithm was used to image the sutures. As a final step, envelope detection was applied to the images to remove the negative values in the image. A maximum amplitude projection (MAP) image is shown in figure 6b. The three sutures are clearly resolved. Additionally, in figure 6c, a MAP image with color coding was applied to locate the suture's z-position relative to the OMUS scanning plane. The green-blue sutures were located at a depth of 2 mm and the the orange-red suture at a depth of 4 mm. All sutures were slightly angled, as seen in the color gradation. The placements of the sutures are accurate representations of the multi-suture phantom. With these results, we believe the OMUSs are capable of imaging more complex targets, such as vasculature in clinical applications.

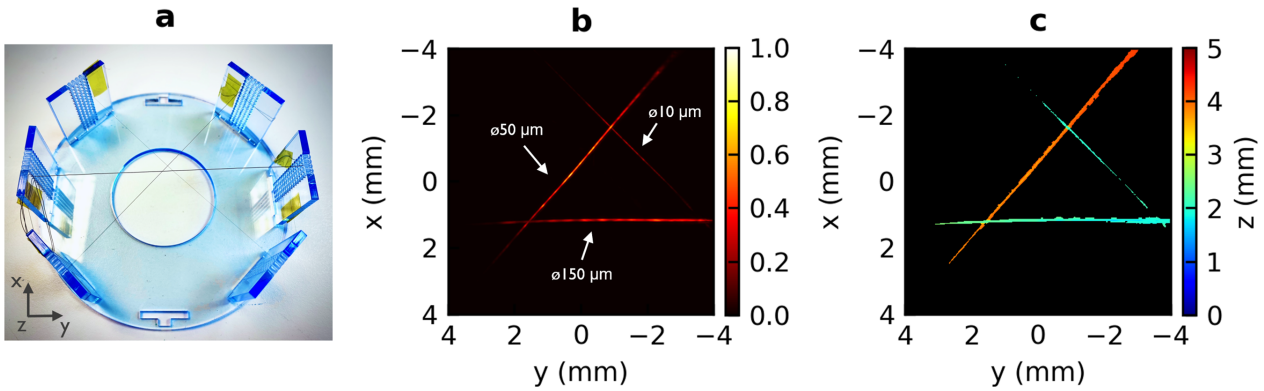

Figure 6. Multi-suture photoacoustic experiment in water. a) Photo of the acrylic suture holder with three different sutures. b) MAP image. c) MAP with depth color encoding.

6. CONCLUSION

We previously demonstrated a sensitive, small, broadband and scalable optomechanical ultrasound sensor (OMUS) implemented in silicon photonics. Here, we studied the OMUS performance for photoacoustic tomography in greater detail. OMUS with different sizes of their acoustically vibrating membranes, and different sensitivity spectra, were studied. These OMUSs with membrane diameters of 25, 21 and 15 µm featured acoustic resonances of 16, 23 and 42 MHz with fractional bandwidths of 52, 55, and 89%, respectively. The OMUSs were applied in photoacosutic imaging on a phantom containing polyamide sutures with a diameter of 10 µm at a depth of 2.5 mm. For the 15 µm OMUS, the axial and lateral image resolution was found as small as 25 and 45 µm, respectively. The corresponding CNR was 55 and limited by imaging algorithm artifacts rather than random noise. Hence, we conclude the OMUS is capable of high-resolution photoacosutic imaging. Based on these results, we believe a fully integrated and multiplexed OMUS array can enable new applications in photoacoustic imaging using on-chip optical ultrasound sensors

ACKNOWLEDGMENTS

CP acknowledges financial support from FWO, Research Foundation - Flanders (project number 1SB8621N).

APPENDIX A. EXPERIMENTAL SETUP

A.1 Optomechanical read-out setup

The OMUS was interrogated around 1550 nm by an external cavity laser (Santec TSL-510) with on-chip power ≈ 0 dBm. The light was TE polarized, coupled through the OMUS, and detected by a photodetector (Newport 1811-FC-AC). The photodetector outputs were captured using an oscilloscope (LeCroy HDO4024A). The two output channels were filtered, with a DC (50 kHz) and an AC output (25 kHz to 125 MHz), corresponding to the transmitted light intensity spectrum and the measured pressure waves, respectively. To tune the laser, the laser was swept with steps of 10 pm across a ring resonance's left flank until the wavelength with the maximum light intensity fluctuations was found, as determined from the noise rms value of the PD AC output. During long experimental measurements, heating and the thermo-optic effect causes the ring resonance to shift.[26] To compensate for this effect, the wavelength was frequently updated to remain at the left flank.

A.2 Photoacoustic setup

Figures 1a-b show the photoacoustic setup. Green pulsed excitation laser light at 532 nm (Innolas SpitLight Compact) was coupled to a fiber bundle (5 mm aperture, CeramOptec). This fiber bundle was placed at a distance of 10 cm from the phantom. The laser light had a pulse width of 6 ns, the pulse repetition rate was set to 15 Hz and the pulse energy was measured around 300-900 µJ (Thorlabs, ES145C) at the sample's distance relative to the fiber bundle. The OMUS was fixated above the phantom and firmly attached to three motorised linear stages with 25 mm travel (Zaber X-LRM025-DEA). In photoacoustic imaging, the OMUS was scanning in a raster pattern, assigning acquired time traces $s(x, y, t)$, unaveraged, to specific sensor coordinates in x and y for later image reconstruction. Since the OMUS was biased on the left flank of the ring resonance, a positive pressure induces a blue shift. Therefore, the acquired signals were inverted prior to imaging.

A.3 Photoacoustic measurement

The photoacoustic signals were measured and acquired by the oscilloscope as time traces, sampled at 500 MHz and shown in figure 7a. The first signal is attributed to stray light hitting the OMUS, invoking a PA response, at the start of the pulsed laser trigger. This signal also had a thermal decay component, that was filtered out with a zero phase bandpass filter with a cutoff at 3MHz. This signal was present in all recording and could be used for time jitter compensation. Here, the edge of the first PA signal was used to align all time traces in post-processing to minimise the time jitter. The second signal in figure 7a, is the PA signal coming from the suture to be imaged, followed by acoustic reflections and time windowed for its first pulse arrival to determine its frequency response. The last window is a noise time trace that comes after the PA signal of the suture. This time window was used to calculate the noise spectral density. The spatial response to a suture placed at 2.5 mm depth relative to the OMUS can be found in figure 7b by linearly scanning in the x-direction over the suture. The spatial response was used as a first estimate in estimating the speed of sound.

A.4 Frequency analysis

The frequency analysis in figure 3d-f was determined as follows. First, the signal spectrum of acquired PA signals were taken with a tukey window of 400, 200 and 100 ns, for membrane diameters of 25, 21 and 15 µm, respectively. These time windows were chosen to select the first pulse arrival. Zero padding was added to the time windows to achieve better resolutions in the frequency domain. Followed by the absolute value of the Fourier transform to estimate the energy spectral density of the PA signals in units mV/Hz. Second, the noise amplitude spectral density was determined by first estimating the noise power spectral density. The noise power spectral density was calculated, using the welch method on small 11 μs time segments on time traces absent of pulsed laser excitation, shown in the last window of figure 7a. The same method was applied to 500 unaveraged noise time traces. Consecutively the noise power spectral densities was averaged in the frequency domain. Averaging of power spectral densities increases the accuracy of the power spectral density estimation. As a final step the square root of the estimated noise spectral density was taken to find the amplitude spectral density in units $\mathrm{mV/Hz^{-1}}$. To find the acoustic resonance frequency and -6 dB bandwidth of the acoustomechanical membranes, the maximum and fwhm of the amplitude spectral density was taken.

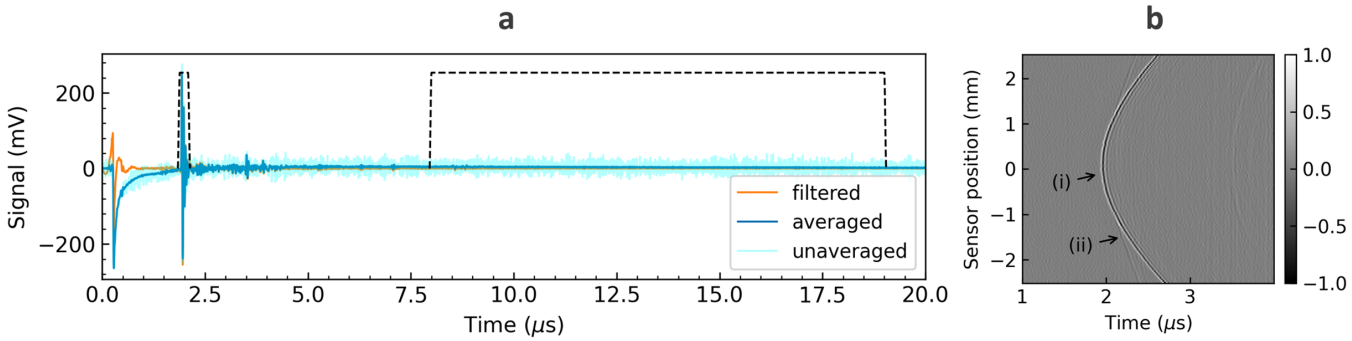

Figure 7. a) Time trace recorded of a 10 µm polyamide suture placed at a distance of 2.5 mm below the 21 µm OMUS b) Spatial response of the OMUS acquired by linearly scanning over the suture in the x-direction. i) Direct ultrasound arrival ii) Arrival through surface wave on OMUS chip.

APPENDIX B. IMAGING ALGORITHM

B.1 Delay and sum

To reconstruct 3D volumetric images, the acquired times traces $s(x, y, t)$ were bandpass filtered, zero phase in the 3-50 MHz frequency range, and back projected using the DAS beamforming technique. In this method, the PA signals are properly aligned using a time delay $\tau(x, y, r) =\mid r - r_{xy}/v_s \mid$, corresponding to the distance between the target at location r and the sensor element position at r_{xy}, and summed over all sensor positions.[25]

$$S_{DAS}(r) = \sum_{x=1}^{N_x} \sum_{y=1}^{N_y} s(x, y, \tau(x, y, r) - d) \tag{1}$$

To find an estimate of the speed of sound and pulse delay, the spatial response of the direct ultrasound wave in figure 7b was used. The least squared fitting method was applied, and a speed of sound of $v_s \approx 1490$ m/s and pulse delay of d ≈ 276 ns was found. For the reconstructed profiles in figures 4 and 5, the negative amplitudes were removed using forced zeroing on the DAS images. The pixels and voxels used in the imaging were 1 μm in size, sufficiently small to accurately calculate a fwhm. The raster imaging scan parameters for photoacoustic imaging can be found in 2.

Table 2. Raster scan imaging used for the spatial resolution characterisation

OMUS	∅25	∅21	∅15	µm
Scanning area	5x5	5x5	5x5	mm^2
Scanning step	37.5	35	18	µm
Sensor positions	133x133	142x142	287x287	

B.2 Delay and sum and coherence factor

To reduce the sidelobe image artifacts in DAS, the DAS image $S_{DAS}(r)$ is multiplied with the coherence factor $CF(r)$. The coherence factor is a nonlinear weighting factor and is defined by the ratio of the square of the coherent and incoherent sum of the aperture data.[25]

$$CF(r) = \frac{(\sum_{x=1}^{N_x} \sum_{y=1}^{N_y} s(x, y, \tau(x, y, r) - d))^2}{N_x N_y \sum_{x=1}^{N_x} \sum_{y=1}^{N_y} s(x, y, \tau(x, y, r) - d)^2} \tag{2}$$

This algorithm was used in figures 5 and 6. As an additional step, the envelope detection was applied in figure 6. This envelope detection is defined by taking the absolute value of the Hilbert transform of the images along the z-axis. This step was also followed by a MAP applied to the volumetric images in the z-direction. In figure 6c, a color coding MAP was applied to locate the suture's position in z relative to the OMUS scanning plane. The voxels used in figure 6 were 10 μm in size.

APPENDIX C. IMAGE ANALYSIS

C.1 Spatial resolution

The spatial resolutions are computed based on the suture profiles in figure 4. The fwhm of the profiles in the lateral and axial direction, illustrated in figure 8a and 8b, correspond to the axial and lateral resolution of the resolved suture, respectively.

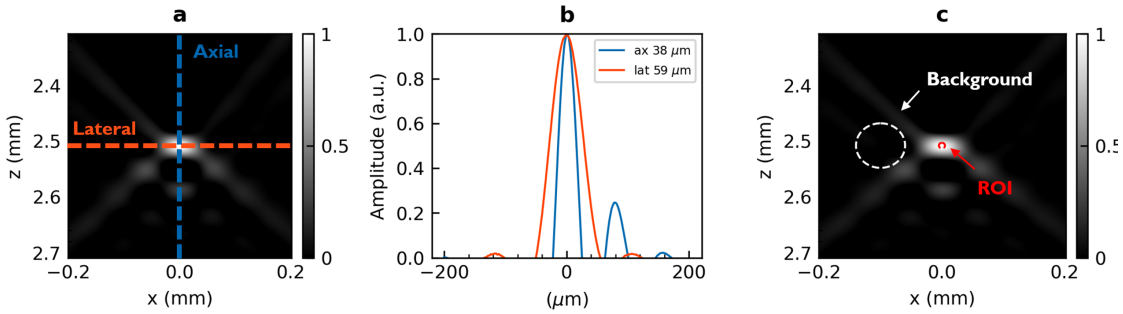

Figure 8. Spatial resolution and CNR characterisation definitions used to evaluate the photoacoustic image of a suture. a) Axial and lateral direction used to compute the spatial resolution. b) ROI and background region used for the CNR calculation.

C.1.1 Image CNR

The CNR was defined as the mean difference between the region of interest (ROI) and a background region divided by the standard deviation of the background.

$$CNR = \frac{\mu_{ROI} - \mu_{Background}}{\sigma_{Background}} \tag{3}$$

In these experiments, a 10 µm region of interest (ROI) was chosen around the position of the 10 µm suture. To define a CNR, this ROI was compared to an 8x times larger background region adjacent to the suture, illustrated in figure 8c.

REFERENCES

[1] Wang, L. V. and Yao, J., "A practical guide to photoacoustic tomography in the life sciences," *Nature Methods* **13**, 627–638 (Aug. 2016).

[2] Ovsepian, S. V., Olefir, I., Westmeyer, G., Razansky, D., and Ntziachristos, V., "Pushing the Boundaries of Neuroimaging with Optoacoustics," *Neuron* **96**, 966–988 (Dec. 2017).

[3] Beard, P., "Biomedical photoacoustic imaging," *Interface Focus* **1**, 602–631 (Aug. 2011).

[4] Attia, A. B. E., Balasundaram, G., Moothanchery, M., Dinish, U., Bi, R., Ntziachristos, V., and Olivo, M., "A review of clinical photoacoustic imaging: Current and future trends," *Photoacoustics* **16**, 100144 (Dec. 2019).

[5] Omar, M., Aguirre, J., and Ntziachristos, V., "Optoacoustic mesoscopy for biomedicine," *Nature Biomedical Engineering* **3**, 354–370 (May 2019).

[6] Olefir, I., Mercep, E., Burton, N. C., Ovsepian, S. V., and Ntziachristos, V., "Hybrid multispectral optoacoustic and ultrasound tomography for morphological and physiological brain imaging," *Journal of Biomedical Optics* **21**, 086005 (Aug. 2016).

[7] Strohm, E. M., Berndl, E. S., and Kolios, M. C., "High frequency label-free photoacoustic microscopy of single cells," *Photoacoustics* **1**, 49–53 (Dec. 2013).

[8] Yao, J. and Wang, L. V., "Photoacoustic microscopy: Photoacoustic microscopy," *Laser & Photonics Reviews* **7**, 758–778 (Sept. 2013).

[9] Zhou, Y., Yao, J., and Wang, L. V., "Tutorial on photoacoustic tomography," *Journal of Biomedical Optics* **21**, 061007 (Apr. 2016).

[10] Winkler, A. M., Maslov, K., and Wang, L. V., "Noise-equivalent sensitivity of photoacoustics," *Journal of Biomedical Optics* **18**, 097003 (Sept. 2013).

[11] Wissmeyer, G., Pleitez, M. A., Rosenthal, A., and Ntziachristos, V., "Looking at sound: Optoacoustics with all-optical ultrasound detection," *Light: Science & Applications* **7**, 53 (Dec. 2018).

[12] Wissmeyer, G., Soliman, D., Shnaiderman, R., Rosenthal, A., and Ntziachristos, V., "All-optical optoacoustic microscope based on wideband pulse interferometry," *Optics Letters* **41**, 1953 (May 2016).

[13] Shnaiderman, R., Wissmeyer, G., Seeger, M., Soliman, D., Estrada, H., Razansky, D., Rosenthal, A., and Ntziachristos, V., "Fiber interferometer for hybrid optical and optoacoustic intravital microscopy," *Optica* **4**, 1180 (Oct. 2017).

[14] Rosenthal, A., Kellnberger, S., Bozhko, D., Chekkoury, A., Omar, M., Razansky, D., and Ntziachristos, V., "Sensitive Interferometric Detection of Ultrasound for Minimally Invasive Clinical Imaging Applications," *Laser & Photonics Reviews* **12**, 1800062 (Apr. 2018).

[15] Guggenheim, J. A., Li, J., Allen, T. J., Colchester, R. J., Noimark, S., Ogunlade, O., Parkin, I. P., Papakonstantinou, I., Desjardins, A. E., Zhang, E. Z., and Beard, P. C., "Ultrasensitive plano-concave optical microresonators for ultrasound sensing," *Nature Photonics* **11**, 714–719 (Nov. 2017).

[16] Jathoul, A. P., Laufer, J., Ogunlade, O., Treeby, B., Cox, B., Zhang, E., Johnson, P., Pizzey, A. R., Philip, B., Marafioti, T., Lythgoe, M. F., Pedley, R. B., Pule, M. A., and Beard, P., "Deep in vivo photoacoustic imaging of mammalian tissues using a tyrosinase-based genetic reporter," *Nature Photonics* **9**, 239–246 (Apr. 2015).

[17] Li, H., Dong, B., Zhang, Z., Zhang, H. F., and Sun, C., "A transparent broadband ultrasonic detector based on an optical micro-ring resonator for photoacoustic microscopy," *Scientific Reports* **4**, 4496 (May 2015).

[18] Cheng Zhang, Sung-Liang Chen, Tao Ling, and Guo, L. J., "Review of Imprinted Polymer Microrings as Ultrasound Detectors: Design, Fabrication, and Characterization," *IEEE Sensors Journal* **15**, 3241–3248 (June 2015).

[19] Zhang, C., Ling, T., Chen, S.-L., and Guo, L. J., "Ultrabroad Bandwidth and Highly Sensitive Optical Ultrasonic Detector for Photoacoustic Imaging," *ACS Photonics* **1**, 1093–1098 (Nov. 2014).

[20] Zarkos, P., Hsu, O., and Stojanović, V., "Ring Resonator Based Ultrasound Detection in a Zero-Change Advanced CMOS-SOI Process," JW2A.78, OSA (2019).

[21] Leinders, S., Westerveld, W., Pozo, J., van Neer, P., Snyder, B., O'Brien, P., Urbach, H., de Jong, N., and Verweij, M., "A sensitive optical micro-machined ultrasound sensor (OMUS) based on a silicon photonic ring resonator on an acoustical membrane," *Scientific Reports* **5**, 14328 (Nov. 2015).

[22] Westerveld, W. J. and Urbach, H. P., [*Silicon Photonics: Electromagnetic theory*], IOP Publishing, Bristol, UK (2017).

[23] Shnaiderman, R., Wissmeyer, G., Ülgen, O., Mustafa, Q., Chmyrov, A., and Ntziachristos, V., "A submicrometre silicon-on-insulator resonator for ultrasound detection," *Nature* **585**, 372–378 (Sept. 2020).

[24] Westerveld, W. J., Mahmud-Ul-Hasan, M., Shnaiderman, R., Ntziachristos, V., Rottenberg, X., Severi, S., and Rochus, V., "Sensitive, small, broadband and scalable optomechanical ultrasound sensor in silicon photonics," *Nature Photonics* **15**, 341–345 (May 2021).

[25] Paul, S., Mandal, S., and Singh, M. S., "Noise adaptive beamforming for linear array photoacoustic imaging," *arXiv:2011.08414 [physics]* (July 2021).

[26] Bogaerts, W., De Heyn, P., Van Vaerenbergh, T., De Vos, K., Kumar Selvaraja, S., Claes, T., Dumon, P., Bienstman, P., Van Thourhout, D., and Baets, R., "Silicon microring resonators," *Laser & Photonics Reviews* **6**, 47–73 (Jan. 2012).